Journal of Power Sources Advances 30 (2024) 100163

Contents lists available at ScienceDirect

Journal of Power Sources Advances

journal homepage: www.sciencedirect.com/journal/journal-of-power-sources-advances

Synergetic effect of double-layer coating on silicon nanoparticles for high-performance lithium-ion battery anodes

Chaerin Gim [a,1], Hyokyeong Kang [a,1], Seungwon Lee [a,1], Gwangeon Oh [a], Shivam Kansara [a], Jang-Yeon Hwang [a,b,c,*]

[a] Department of Energy Engineering, Hanyang University, Seoul, 04763, Republic of Korea
[b] Department of Battery Engineering, Hanyang University, Seoul, 04763, Republic of Korea
[c] Center for Energy Storage System, Chonnam National University, Gwangju, 61186, Republic of Korea

ARTICLE INFO

Keywords:
Silicon
Anodes
High capacity
Double-layer coating
Lithium-ion batteries

ABSTRACT

Silicon has emerged as a potential candidate for next-generation lithium-ion battery (LIB) anodes owing to its exceptionally high theoretical capacity (3580 mAh g^{-1}) and environmental abundance. However, the practical application of Si anodes is severely hindered by low electrical conductivity and a substantial volume expansion rate of over 300 % during the lithiation–delithiation process, leading to rapid capacity degradation. To address these challenges, a double-layer coating strategy was developed and successfully applied to simultaneously enhance the electrical conductivity and mechanical integrity of Si nanoparticles (Si). The double coating layer was designed with an inside conductive pathway and outside robust coverage, which was achieved by encapsulating silicon with a conductive amorphous carbon layer on the silicon surface and coating it with a TiO_2 layer (Si@C@TiO_2). These features improved the interfacial and structural stability of the electrodes during repeated cycling. Compared with its respective uncoated and single-coated analogous anodes, the Si, carbon-coated Si (Si@C), and TiO_2-coated Si (Si@TiO_2) anodes, the Si@C@TiO_2 anode demonstrates exceptional cycling stability and power capability. We believe that this study offers a breakthrough in the design of high-performance Si-based anodes for LIBs.

1. Introduction

Over the past two decades, the increasing demand for high-capacity lithium-ion batteries (LIBs) has driven extensive research on new electrode materials to meet the requirements of portable electronics, hybrid electric vehicles, and large-scale energy storage systems. To improve the energy density of LIBs, metals and semimetals have emerged as promising alternatives to traditional carbonaceous anodes because they can deliver high specific capacities by forming electrochemical alloys with lithium [1–3]. Among these, silicon is the leading candidate due to its abundance in the Earth's crust and the remarkably high theoretical capacity of its fully lithiated state (3580 mAh g^{-1}), approximately 10 times greater than that of natural graphite (372 mAh g^{-1}) [4,5]. However, the practical application of Si anodes is hindered by significant challenges, primarily the dramatic volume change (>300 %) that occurs during lithiation and delithiation [6–10]. Volume expansion induces mechanical stress, leading to pulverization of the particle, formation of an unstable solid–electrolyte interphase (SEI) layer, loss of electrical contact, rapid capacity fading, and safety issues [11–13]. To address these issues, extensive research has focused on improving the electrochemical performance of Si-based anodes through various approaches that can better accommodate volume changes and enhance cyclability. The primary approach is the nanostructuring of Si particles [12–18]. Reducing the Si particle size to the nanoscale effectively reduces the mechanical stress caused by significant volume changes. Composites of Si with a buffer matrix have also become a key focus, particularly Si/C composites [19–22]. These composites combine the high capacity of Si with the excellent conductivity and structural stability of carbon, resulting in improved electrical conductivity and the ability to buffer volume changes and further improve cycling performance [23]. Another effective strategy involves the application of various coatings onto the Si particles. For example, coating with metal oxides such as TiO_2, Al_2O_3, and ZnO offers robust mechanical integrity and protects the Si particles from direct contact with the acidic electrolyte solution [24–27]. Despite

* Corresponding author. Department of Energy Engineering, Hanyang University, Seoul, 04763, Republic of Korea.
E-mail address: jangyeonhw@hanyang.ac.kr (J.-Y. Hwang).
[1] These authors contributed equally to this work.

https://doi.org/10.1016/j.powera.2024.100163
Received 2 October 2024; Received in revised form 1 November 2024; Accepted 13 November 2024
Available online 21 November 2024

these advancements, however, existing approaches still face limitations. One of the key challenges is the trade-off between capacity and cycling stability; although some techniques improve cycling performance, they often do so at the expense of the specific capacity and/or power capability [28]. Addressing these gaps is essential for developing efficient, advanced solutions to enhance the performance of Si-based anodes in commercial LIBs [29–31].

In this study, we introduce a simple, effective strategy to improve the electrochemical properties of Si-based anodes via a double-layer coating. The double-layer coating comprised an inner conductive pathway and outer robust coverage, achieved by encapsulating a conductive carbon layer on the Si surface and coating it with an anatase TiO_2 layer. This double-layer coating reinforces the structural and interfacial stability of Si nanoparticles (Si) by suppressing huge volume changes and preventing the direct exposure of Si to the electrolyte. As a result, the proposed Si@C@TiO₂ anode delivered a high capacity of 2200 mAh g^{-1} and demonstrated good cycling stability over 100 cycles at 0.2C.

2. Experimental section

2.1. Materials

2.1.1. Preparation of Si@C, Si@TiO_2, and Si@C@TiO_2

Si powder (600 mg; CNVISON Co., Ltd.) was dispersed in deionized (DI) water using 3 mL of 20 % cetyltrimethylammonium bromide (CTAB, Sigma–Aldrich) as a surfactant. Vigorous stirring at room temperature for 1 h produced Si@CTAB as a powder, which was dried overnight in a convection oven at 80 °C. The Si@CTAB powder (500 mg) was added to Tris-buffer solution (pH = 8.5), and then the solution was ultrasonicated at 30 % amplitude for 10 min (Solution A). Dopamine hydrochloride (500 mg; 99 %, Alfa Aesar) was dissolved in DI water and slowly added to Solution A. After stirring for 24 h at room temperature, Si@PDA powder was collected by washing with DI water and ethanol (EtOH). To synthesize the Si@C sample, the powder was carbonized at 800 °C under an Ar atmosphere for 2 h. To synthesize Si@TiO_2 or Si@C@TiO_2, hydroxypropyl cellulose (0.5 g) was dissolved in EtOH at 90 °C with vigorous stirring for 0.5 h (Solution B). Then, 100 mg of Si powder (or Si@C) was added to Solution B, and the mixture was ultrasonicated for dispersion (Solution C). After that, 2 mL H_2O was added slowly to Solution C (Solution D). Finally, titanium butoxide (TBOT, Sigma–Aldrich, 97 %) was dissolved in EtOH and injected into Solution D drop by drop. After washing using DI water and EtOH, the obtained powder was calcined at 500 °C under an Ar atmosphere for 3 h.

2.2. Material characterizations

X-ray diffraction (miniFlex600, Rigaku) and Raman spectrometry (DXR3xi, Thermo Fisher) were used to analyze the crystal structures of the Si@C@TiO_2 samples. The surface morphology of the material was characterized by scanning electron microscopy (SEM, Helios, FEI). Transmission electron microscopy (TEM, JEM 2100F, JEOL) and TEM-EDX data were also measured (JEM 2100F, JEOL). The sample chemical states were analyzed using X-ray photoelectron spectroscopy (XPS; XPS-Theta Probe, Thermo Scientific Co.). Thermal gravimetry analyses (TGA) (SDT Q600, TA Instruments) were performed under air flow with a 10 °C min^{-1} heating temperature ramp to quantify the carbon content in the samples. Cross-sectional Si, Si@C, Si@TiO_2, and Si@C@TiO_2 anodes were prepared using an Ar-ion beam cross-section polisher (CCP; IB-19520CCP; JEOL, Ltd.).

2.3. Electrochemical tests

To fabricate Si, Si@C, Si@TiO_2, and Si@C@TiO_2 anodes, the active material was mixed with Super P and 6 wt% polyacrylic acid (PAA) in DI water at the ratio 6:2:2. The resulting slurry was coated onto a carbon-coated Cu foil using a doctor blade and dried in a convection oven at 60 °C for 12 h. The mass loading was approximately 1–1.5 mg cm^{-2}. The electrochemical properties of the Si, Si@C, Si@TiO_2, and Si@C@TiO_2 anodes were evaluated by assembling CR2032 coin-type half-cells using Li metal as the counter electrode and a polypropylene membrane (Celgard 2400) as the separator. The electrolyte consisted of 1 M $LiPF_6$ dissolved in a solvent mixture of ethylene carbonate and diethyl carbonate (1:1, v/v) with 5 wt% fluoroethylene carbonate (Enchem Co., LTD.). Galvanostatic charge–discharge cycling was performed between 0.01 and 1.5 V using a WBCS3000 (WonA Tech) system. The current rate was 1 C = 2000 mA g^{-1} for half-cells. Electrochemical impedance spectroscopy (EIS) measurements were carried out over a frequency range of 1 MHz–10 mHz at 10 mV amplitude using VMP-3e (Bio-Logic SAS).

3. Results and discussion

3.1. Synthesis and characterization of double-layer coated Si

This work proposes a double-layer coating strategy to enhance the reversible Li^+ storage properties of Si as an anode. Fig. S1 depicts the synthetic procedure of Si@C@TiO₂ powder. In nature, the surface of Si powder is oxidized by forming a SiO_2 layer with hydroxyl groups (–OH) [32]. In addition, Si powders are generally aggregated owing to their high surface energy [33] and are thus difficult to disperse in water. For uniform Si powder dispersion in water, we modified the surface of the Si powder by introducing cetyltrimethylammonium bromide (CTAB) as a surfactant into the solution (Fig. S2). For the carbon coating of the surface, the Si powders modified with CTAB (Si@CTAB) were uniformly dispersed in a Tris-buffer solution (pH = 8.5). Dopamine hydrochloride was added to the solution, and the well-dispersed Si@CTAB powder was encapsulated by polydopamine (PDA) through a spontaneous polymerization process (Si@PDA). The Si@PDA powder was calcined at 800 °C under an Ar atmosphere for 2 h. During heat treatment, CTAB and PDA on the surface of the Si powder were pyrolyzed to form an amorphous carbon layer (Si@C). The effect of CTAB can be clearly seen in Fig. S3, where the Si@C with CTAB showed even particle distributions without particle agglomeration and uniform carbon coating of 5.42 nm on Si surface. On the other hand, Si@C particles without CTAB showed agglomeration of the particles with thicker (11.16 nm) carbon coating layer. This suggested that introduction of CTAB in the synthetic procedure of Si@C ensured effective nanoparticle stabilization and allowed us to achieve the desired uniform carbon coating on Si particles. Finally, the Si@C powder surface was coated by an anatase TiO_2 layer through the sol–gel method, using titanium butoxide and following heat treatment at 500 °C under an Ar atmosphere for 3 h.

The Si, Si@C, and Si@TiO_2 samples were initially characterized to validate the successful synthesis of the double-layer coating on their surfaces. The X-ray diffraction (XRD) patterns of the Si samples showed distinct peaks corresponding to crystalline Si (Fig. S4a). Upon coating with carbon, the XRD pattern showed the persistence of amorphous carbon and Si peaks in the carbon layer (Fig. S4b). When the Si was coated with TiO₂, the XRD pattern clearly showed the presence of anatase TiO₂ along with Si peaks, indicating the successful formation of the TiO₂ layer (Fig. S4c). SEM images showed that the Si sample had a nanowire morphology connected by spherical particles with diameters of 20–100 nm (Fig. S5a). After carbon coating, a slight increase in the particle diameter, but with a smooth surface, was observed owing to the presence of the carbon layer on the Si sample surface (Fig. S5b). After TiO_2 coating, the particle diameter increased noticeably, and the particle surfaces became intertwined owing to the presence of a crystalline medium compared to the Si and Si@C samples (Fig. S5c). For the XRD pattern of the Si@C@TiO₂ sample (Fig. 1a), the distinct peaks corresponding to Si were well-aligned (JCPDS No. 00-026-1481), confirming that the crystalline structure of Si was preserved throughout the synthesis process [34,35]. Additionally, a broad peak representing

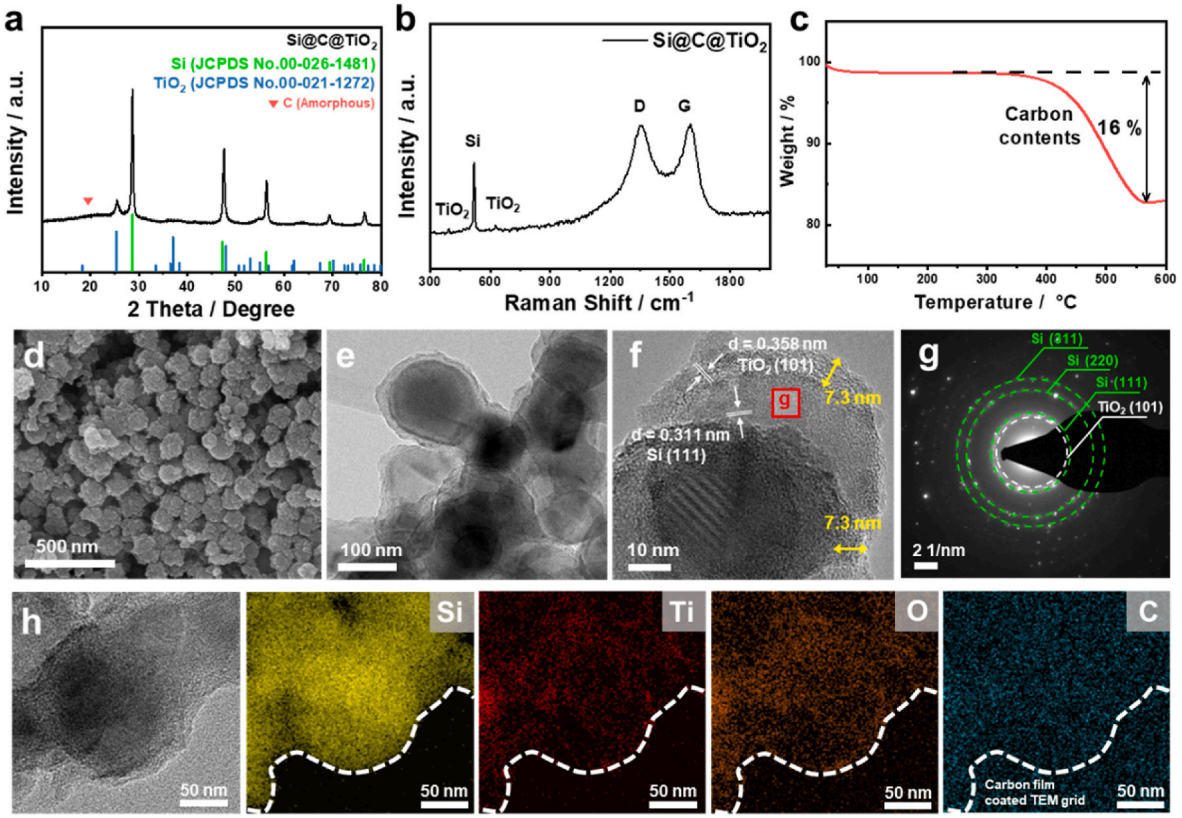

Fig. 1. Characterizations of the Si@C@TiO_2 sample: (a) XRD patterns (b) Raman spectra, (c) TGA plot, (d) SEM image, (e) bright-field TEM image, (f) HR–TEM image, (g) SAED pattern marked region in (f), (h) HR-TEM image and corresponding EDX mapping.

amorphous carbon appeared in the 20°–25° range [36]. The presence of anatase TiO_2 was confirmed by peaks matching the standard anatase phase TiO_2. The Raman spectroscopy analysis further corroborated the structural integrity of the Si@C@TiO_2 sample. In the Raman spectra, the peaks for the D-band (~1350 cm^{-1}) and G-band (~1580 cm^{-1}) of amorphous carbon and peaks associated with Si (~501 cm^{-1}) and TiO_2 (~395 and 636 cm^{-1}) were observed (Fig. 1b) [37,38]. A combined study of XRD and Raman analysis verified the successful fabrication of Si@C@TiO_2 with all intended components coexisting and correctly integrated [38]. Thermogravimetric analysis (TGA) data (Fig. 1c) confirmed the carbon content (~16 %) in the Si@C@TiO_2 sample. The weight loss of about 2 wt% of Si@C@TiO_2 up to 150 °C in TGA curve is related to the desorption of adsorbed water. Although Si particles are oxidized in air, the dense oxide film on the surface prevents further oxidation, so that the weight of the Si powder raw material is almost constant at 150–600 °C [39,40]. A significant weight loss of Si@C@TiO_2 occurs in the temperature range of 350–560 °C, which is attributed to the oxidation of carbon in Si@C@TiO_2. Compared to the Si, Si@C, and Si@TiO_2 samples, the SEM and bright-field transmission electron microscopy (TEM) images in Fig. 1d and **e** showed that the Si@C@TiO_2 sample has a relatively large particle size owing to the double-layer coating. High–resolution TEM (HR–TEM) confirmed the presence of an amorphous carbon layer (thickness: ~7 nm), along with d-spacings of 0.311 nm and 0.358 nm. These lattice fringe spacings correspond to the (111) plane of Si and the (101) plane of anatase TiO_2, respectively, as determined from the XRD pattern using Bragg's law. This further validates the structure of the synthesized Si@C@TiO_2 composite. This further validates the structure of the synthesized Si@C@TiO_2 composite.

Selected area electron diffraction (SAED) patterns for the marked region in the HR-TEM image showed the distinct diffraction rings corresponding to the Si (111) plane and the TiO_2 (101) plane. In addition, energy dispersive X-ray spectroscopy (EDX) analysis in conjunction with HR–TEM confirmed that a uniform carbon layer and a TiO_2 layer surround the Si samples. The final composition of Si@C@TiO_2 was calculated to be 65:16:19 by TEM-EDX and TGA analyses. X-ray photoelectron spectroscopy (XPS) analysis was also conducted to characterize the chemical composition of the Si@C@TiO_2 surface. The intense peak in the C 1s spectrum could be deconvoluted into three peaks: Si−C, C−C, and C−OH peaks were detected at 284.3, 284.8, and 285.6 eV, respectively [41,42]. These peaks indicated the formation of an amorphous carbon coating layer on the Si surface. The Si 2p spectra were also deconvoluted into three peaks with binding energies of 103.7 eV (SiO_x), 102.6 eV (Si–O–C), and 99.4 eV (Si–Si), respectively [43,44]. It should be noted that a SiO_x film was generally observed on the surface of the Si samples owing to natural oxidation. The presence of the SiO_x film was also confirmed by the HR-TEM images of the Si samples (Fig. S6a). Two intensified peaks with binding energies of 459.8 and 453.9 eV were observed in the Ti 2p spectra (Fig. S7) [45,46]. These peaks correspond to Ti $2p^{3/2}$ and Ti $2p^{1/2}$ of Ti^{4+}, confirming the presence of TiO_2 on the surface of the Si@C@TiO_2 sample.

3.2. Electrochemical performance

To confirm the benefits of the double-layer coating, the electrochemical performances of the Si, Si@C, Si@TiO_2, and Si@C@TiO_2 anodes were evaluated using CR2032-type coin cells, and the results are compared in Fig. 2. All cells were tested in the voltage range of 0.01–1.5 V (vs. Li/Li^+) at 30 °C. All samples showed typical voltage profiles of the Si-based anode in the first cycle at 0.1C, suggesting that the Si anodes were well preserved during the single- or double-layer coating process. The Si anodes delivered a high specific capacity of 2200 mAh g^{-1} at 0.1C. For the cycling test at 0.2C, the Si anode showed rapid capacity fading during 100 cycles, which is a direct consequence of huge volume changes during the alloying−dealloying process. Compared to the Si

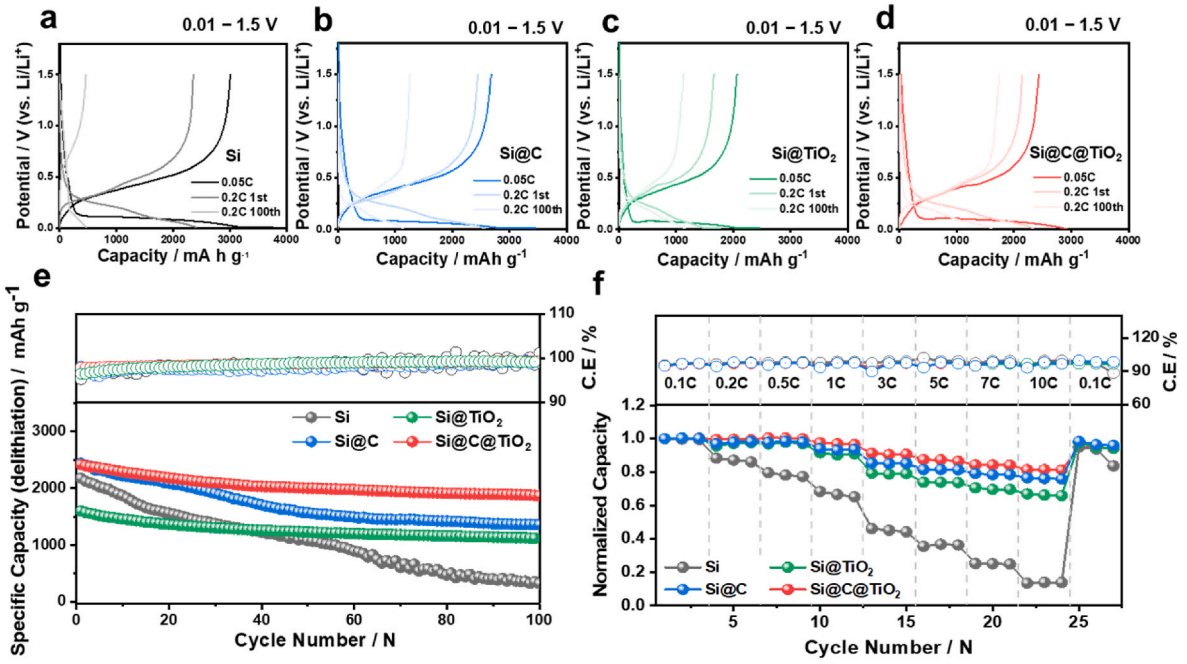

Fig. 2. The charge/discharge curves of (a) Si, (b) Si@C, (c) $Si@TiO_2$, and (d) $Si@C@TiO_2$ anodes at 0.05C (CC-CV) and 0.2C (CC); (e) Specific delithiation capacity vs. cycle number of Si, Si@C, $Si@TiO_2$, and $Si@C@TiO_2$ anodes at 0.2C; (f) normalized capacity variation at various current densities from 0.1 to 10 C of Si, Si@C, $Si@TiO_2$ and $Si@C@TiO_2$ anodes.

anode, the Si@C anode exhibited an enhanced specific capacity of 2600 mAh g^{-1} at 0.1C and cycling stability at 0.2C. The carbon coating layer provided a conductive network that helped maintain electrical contact between the Si particles and functioned as a mechanical buffer, accommodating some of the volume changes during cycling. Nonetheless, the Si@C anode still experienced continuous capacity fading during cycling, indicating that the carbon coating was not fully effective in preventing degradation of the Si anode associated with a large volume change. The TiO_2 coating, known for its mechanical strength and chemical stability, provides a robust protective layer surrounding the Si sample, suppressing the volume expansion rate and preventing the electrolyte decomposition at the particle surface. Owing to the insulating nature of TiO_2, the $Si@TiO_2$ anode delivered a relatively lower specific capacity of 1700 mAh g^{-1} at 0.1C but exhibited significantly enhanced cycling stability compared to the Si and Si@C anodes. By combining the advantages of both carbon and TiO_2 coatings, a significant improvement in electrochemical properties was observed in the $Si@C@TiO_2$ anode (Fig. 2d). The $Si@C@TiO_2$ anode delivered a high specific capacity of 2300 mAh g^{-1} at 0.2C, which is the compatible value with the Si anode even after double coating. For the cycling test at 0.2C, the $Si@C@TiO_2$ anode retained a high specific capacity of over 2000 mAh g^{-1} after 100 cycles, significantly outperforming the other anodes. Fig. S8 compares the Nyquist plots of the Si and $Si@C@TiO_2$ anodes after 100 cycles at 0.2C. The $Si@C@TiO_2$ anode exhibited more than three times lower charge-transfer resistances (R_{ct}) (40.1 Ω) than the Si anode (133.6 Ω), demonstrating that the double-layer coating contributes to a facile lithium-ion transport from the surface to the particle bulk. Moreover, the $Si@C@TiO_2$ anode delivered the highest capacity retention of 82 %, even at 10 C, demonstrating excellent power capability (Fig. 2f and Fig. S9). These superior performances of the $Si@C@TiO_2$ anode could be attributed to the combined effects of the carbon coating, which enhances electrical conductivity, and the TiO_2 layer, which provides mechanical robustness and chemical stability. In other words, in comparison, the Si@C and $Si@TiO_2$ anodes, while better than a pure Si anode, exhibited inferior cycling stability or lower capacity than the $Si@C@TiO_2$ anode; this indicated the limitations of single-layer coating for effectively addressing the critical issues of Si anodes. Differential capacity (dQ dV^{-1}) analysis provided further insights into the different anode stabilities. Note that in the dQ dV^{-1} vs. voltage plots, the peaks correspond to specific processes related to the phase equilibria during the charge–discharge process. Thus, dQ dV^{-1} adequately describes the electrochemical response, particularly the reversibility of the redox reactions in typical charge–discharge voltage profiles. All samples showed the typical redox features of the Si anode in LIBs (Fig. S10). During the early lithiation process, the peaks at approximately 0.21 V indicate that the Si structure changed from crystalline to amorphous phase. A sharp reduction peak appeared at 0.2–0 V, indicating that multiple Li_xSi phases coexisted because of the alloying reaction during the deep lithiation process. During the delithiation process, the peaks at 0.3 and 0.5 V were observed by dealloying reaction. The comparison data of dQ dV^{-1} at the first and 100th cycles for each sample further confirmed that the double-layer coating substantially improved the reversible alloying–dealloying reaction of Si by minimizing the structural degradation during long-term cycling.

3.3. Mechanistic insights

Fig. 3 compared the cross-sectional SEM images of the Si, Si@C, $Si@TiO_2$, and $Si@C@TiO_2$ anodes (prepared with cross-section polisher) before and after cycle (dealloying state at 1.5 V). In the pristine state, the Si electrode appears to be much more porous than the other samples (Fig. 3a–d). Si nano powders typically aggregate due to their high surface energy. This aggregation can lead to a non-uniform structure within the electrode, increasing voids. However, the coated nano powders demonstrate a greater reduction in agglomeration compared to uncoated Si, which appears to lower porosity within the electrode. After 100 cycles (Fig. 3e–h), the Si anode exhibited severe structural deterioration with deep cracks and significant pulverization, which could be attributed to the notorious volume changes during multiple alloying–dealloying reactions. This mechanical degradation leads to the loss of electrical contact between Si and the conductive carbon in the electrode, resulting in rapid capacity fading [47]. The Si@C anode demonstrates a noticeable improvement in structural integrity compared to the Si anode after 100 cycles. The carbon coating provides a

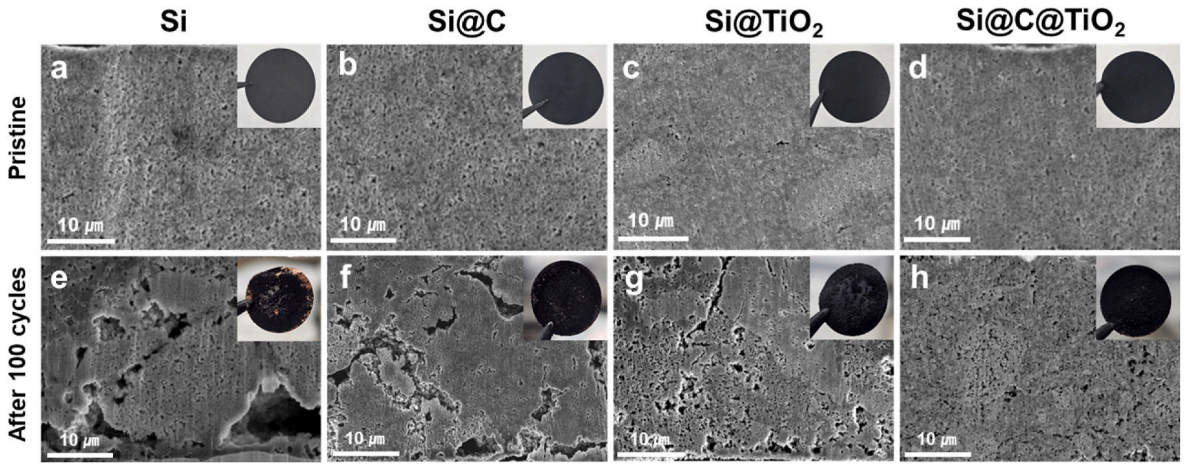

Fig. 3. Cross-sectional SEM images of the pristine state of (a) Si, (b) Si@C, (c) Si@TiO_2, and (d) Si@C@TiO_2 anodes; and after 100th cycling of (e) Si, (f) Si@C, (g) Si@TiO_2, and (h) Si@C@TiO_2 anodes (inset: digital photographs of electrodes corresponding to SEM images).

uniform electrical pathway and acts as a mechanical buffer layer, reducing the localization of current distribution and suppressing Si volume changes. The Si@TiO_2 anode remained relatively intact with fewer, shallower cracks than the Si and Si@C anodes due to its mechanically robust inorganic TiO_2 particles. Strikingly, the Si@C@TiO_2 anode displayed minimal signs of cracking or degradation, indicating that double-layer coating effectively prevented the mechanical failure associated with huge Si volume changes, thereby contributing to better cycling stability. These features are directly related to the adhesion strength of the electrode. The trends observed in cross-sectional SEM images can be found in the surface conditions (digital photographs) of the cycled electrode. The Si anode displayed significant surface roughness and visible material loss. The Si@C (Fig. 3f) and Si@TiO_2 (Fig. 3g) anodes, while in better condition than the pure Si anode, still exhibited imperfect surfaces with some cracks, indicating that single-layer coating did not provide efficient protection. In contrast, the Si@C@TiO_2 anode (Fig. 3h) showed a remarkably smooth surface with minimal signs of degradation. However, structural differences between the samples also change the interfacial stability. Typically, when a large volume change occurs in a Si-based anode, the anode surface becomes rough and cracked as the alloying–dealloying process is repeated. Worse, electrolyte solution easily penetrates along the cracks into the electrode interior, continuously exposing active material. These phenomena accelerate the electrolyte decomposition inside and outside the electrode, resulting in a thick, SEI layer.

To compare the electrolyte decomposition level between the samples, the chemical compositions of the SEI layer were analyzed through XPS measurements after 100 cycles at 0.2C (Fig. 4). The C 1s and O 1s XPS profiles typically represent the decomposition of solvent molecules. Note that in the C 1s spectra, the peaks at ~285 eV correspond to the C–C bond originating from the electrode conductive carbon (Super P) or polymeric binder (PAA), and the peak at 286.5 eV corresponds to C–O/C–F bonds decomposed by the fluoroethylene carbonate (FEC) [48–51]. The C 1s peaks at ~288.7 eV and ~290 eV correspond to the O=C–O and O–(C=O)–O such as in lithium alkyl carbonates ($LiCO_3R$) and lithium carbonate (Li_2CO_3); the O 1s peaks at ~530.9, ~530.5, ~529.5, and ~531.8 eV correspond to C–O/H–O, R–O–Li, Li_2O, and C=O [52–55]. These compounds are typically formed by decomposing ethylene carbonate (EC) and diethyl carbonate (DEC) solvents. Compared to the other samples, the SEI layer on the Si@C@TiO_2 anode showed the lowest fraction of all compounds. These results clearly suggest that the double-layer coating greatly suppressed the electrolyte solution decomposition by relaxing the structural stress and inhibiting the direct contact of Si with the electrolyte solution.

Based on the cross-sectional SEM analysis and XPS data, Fig. 5 summarizes the effect of the double-layer coating on the Li^+ storage

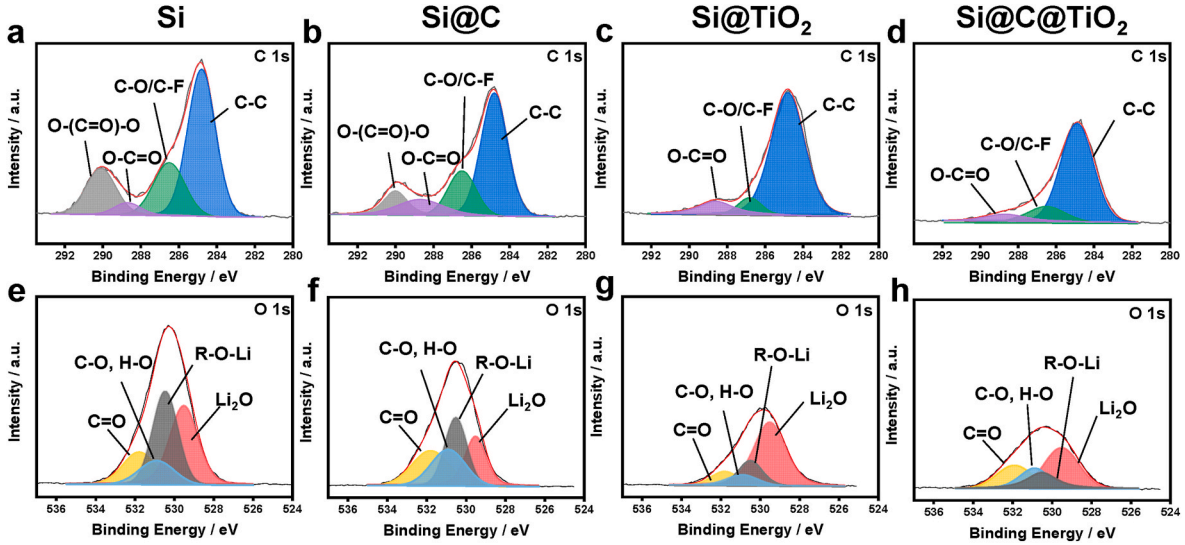

Fig. 4. XPS spectra for C 1s and O 1s for (a, e) Si, (b, f) Si@C, (c, g) Si@TiO_2, and (d, h) Si@C@TiO_2 after 100 cycles at 0.2C.

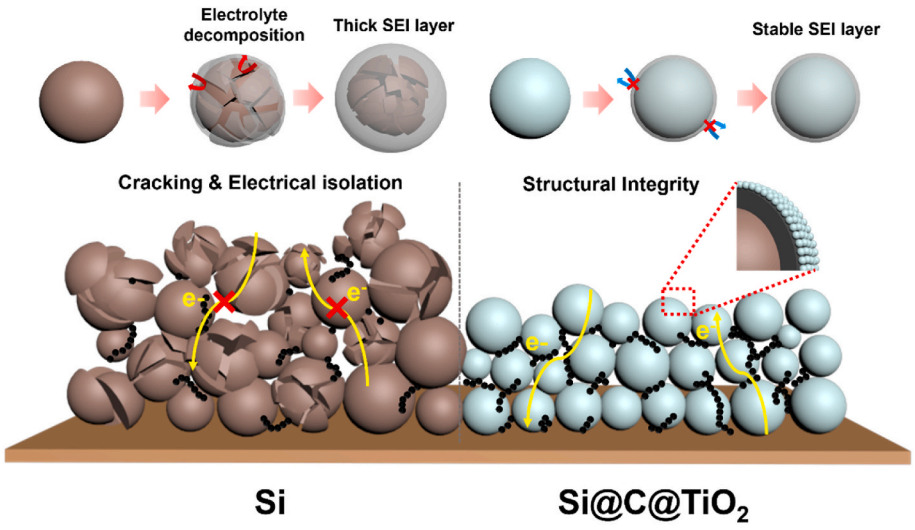

Fig. 5. Summary of the functions of the double-layer coating to improve the Li^+ storage properties of Si.

properties of the Si anode. The significant Si volume changes during cycling cause the Si anode to crack and disintegrate, propagating to the electrode level. This leads to electrical contact loss among Si atoms within the electrode and accelerates electrolyte decomposition, forming a thick SEI layer. In contrast, the double-layer coating helps to maintain the structural integrity of Si during cycling by preventing the core particles from cracking, improving the mechanical stability of the electrode. In addition, the SEI layer on the Si@C@TiO_2 anode remains conformal, uniformly covering the particle surfaces without breaking apart. As a result, the Si@C@TiO_2 anode can deliver superior Li^+ storage properties compared to other samples [56].

4. Conclusion

In this paper, we propose a double-layer coating strategy to enhance the electrochemical Li^+ storage properties of Si as an anode material for LIBs. The double-layer coating is designed with an inside conductive pathway and robust outside coverage, achieved by encapsulating a conductive amorphous carbon layer on the Si surface and further coating it with an anatase TiO_2 layer (Si@C@TiO_2). A Si@C@TiO_2 sample was successfully synthesized through dopamine polymerization, carbonization, and the sol–gel method for TiO_2 coating. The double-layer coating provided robust conductive pathways for rapid electron transport and mechanical integrity to prevent the cracking and pulverization of the Si core. The unique features guarantee the interfacial stability of Si@C@TiO_2 against electrolyte solution from particle to electrode level, suppressing the irreversible electrolyte decomposition. As a result, the Si@C@TiO_2 anode exhibited better cycling stability and power capability compared with the Si, Si@C, and Si@TiO_2 anodes. We believe that the proposed double-layer coating strategy will facilitate the development of high-performance Si-based anode materials.

CRediT authorship contribution statement

Chaerin Gim: Writing – original draft, Visualization, Data curation, Conceptualization. **Hyokyeong Kang:** Writing – original draft, Resources, Investigation, Formal analysis. **Seungwon Lee:** Validation, Formal analysis. **Gwangeon Oh:** Resources, Data curation. **Shivam Kansara:** Visualization, Validation. **Jang-Yeon Hwang:** Writing – review & editing, Supervision, Conceptualization.

Declaration of competing interest

The authors declare that they have no known competing financial interests or personal relationships that could have appeared to influence the work reported in this paper.

Acknowledgments

This work was supported by the National Supercomputing Center with supercomputing resources including technical support (KSC-2024-CRE-0109) and the Agency for Defense Development by the Korean Government (UD2200061D).

Appendix A. Supplementary data

Supplementary data to this article can be found online at https://doi.org/10.1016/j.powera.2024.100163.

Data availability

Data will be made available on request.

References

[1] A. Rakhmetova, A. Belgibayeva, G. Kalimuldina, A. Nurpeissova, Z. Bakenov, Free-standing SnSe@C nanofiber anode material for low-temperature lithium-ion batteries, J. Power Sources Adv 24 (2023) 100128, https://doi.org/10.1016/j.powera.2023.100128.
[2] J. Lee, G. Oh, H.-Y. Jung, J.-Y. Hwang, Silicon anode: a perspective on fast charging lithium-ion battery, Inorganics 11 (2023) 182, https://doi.org/10.3390/inorganics11050182.
[3] L. Zhou, J. Zhang, Y. Wu, W. Wang, H. Ming, Q. Sun, L. Wang, J. Ming, H. N. Alshareef, Understanding ostwald ripening and surface charging effects in solvothermally-prepared metal oxide–carbon anodes for high performance rechargeable batteries, Adv. Energy Mater. 9 (2019) 1902194, https://doi.org/10.1002/aenm.201902194.
[4] M. Nie, D.P. Abraham, Y. Chen, A. Bose, B.L. Lucht, Silicon solid electrolyte interphase (SEI) of lithium ion battery characterized by microscopy and spectroscopy, J. Phys. Chem. C 117 (2013) 13403–13412, https://doi.org/10.1021/jp404155y.
[5] M.N. Obrovac, L.J. Krause, Reversible cycling of crystalline silicon powder, J. Electrochem. Soc. 154 (2007) A103–A108, https://doi.org/10.1149/1.2402112.
[6] M.N. Obrovac, L. Christensen, Structural changes in silicon anodes during lithium insertion/extraction, Electrochem. Solid State Lett. 7 (2004) A93, https://doi.org/10.1149/1.1652421.
[7] B. Hertzberg, A. Alexeev, G. Yushin, Deformations in Si-Li anodes upon electrochemical alloying in nano-confined space, J. Am. Chem. Soc. 132 (2010) 8548–8549, https://doi.org/10.1021/ja1031997.
[8] L. Shi, W. Wang, A. Wang, K. Yuan, Y. Yang, Facile synthesis of scalable pore-containing silicon/nitrogen-rich carbon composites from waste contact mass of organosilane industry as anode materials for lithium-ion batteries, J. Mater. Chem. A 2 (2014) 20213–20220, https://doi.org/10.1039/C4TA03561E.
[9] T. Cai, W. Wahyudi, P. Kumar, Z. Ma, Q. Sun, H. Xie, Y. Wang, F. Zhao, Z. Cao, L. Cavallo, Q. Li, J. Ming, Overlooked challenges of interfacial chemistry upon

developing high energy density silicon anodes for lithium-ion batteries, Mater. Sci. Eng. R Rep. 161 (2024) 100854, https://doi.org/10.1016/j.mser.2024.100854.
[10] H. Xue, Y. Wu, Y. Zou, Y. Shen, G. Liu, Q. Li, D. Yin, L. Wang, J. Ming, Unraveling metal oxide role in exfoliating graphite: new strategy to construct high-performance graphene- modified SiOx-based anode for lithium-ion batteries, Adv. Funct. Mater. 30 (2020) 1910657, https://doi.org/10.1002/adfm.201910657.
[11] A. Magasinski, P. Dixon, B. Hertzberg, A. Kvit, J. Ayala, G. Yushin, High-performance lithium-ion anodes using a hierarchical bottom-up approach, Nature Mater 9 (2010) 353–358, https://doi.org/10.1038/nmat2725.
[12] Y. Jin, B. Zhu, Z. Lu, N. Liu, J. Zhu, Challenges and recent progress in the development of Si anodes for lithium-ion battery, Adv. Energy Mater. 7 (2017) 1700715, https://doi.org/10.1002/aenm.201700715.
[13] H. Xue, Y. Wu, Z. Wang, Y. Shen, Q. Sun, G. Liu, D. Yin, L. Wang, Q. Li, J. Ming, Unraveling the new role of Metal−Organic frameworks in designing silicon hollow nanocages for high-energy lithium-ion batteries, ACS Appl. Mater. Interfaces 13 (2021) 40471–40480, https://doi.org/10.1021/acsami.1c07495.
[14] M. Yasoubi, A. Habibi, S. Hoornam, Z. Sanaee, S. Mohajerzadeh, Superior performance of silicon nanowires@void@carbon on a conductive substrate as a scalable binder-free anode electrode for lithium-ion batteries, Sustain. Energy Fuels 8 (2024) 3419–3437, https://doi.org/10.1039/D4SE00314D.
[15] G. Farid, R. Amade-Rovira, R. Ospina, E. Bertran-Serra, Surface modification of silicon nanowires via drop-casting for high-performance Li-ion battery electrodes: SiNWs decorated with molybdenum oxide nanoparticles, J. Energy Storage 78 (2024) 110104, https://doi.org/10.1016/j.est.2023.110104.
[16] Y. Yang, W. Yuan, W. Kang, Y. Ye, Y. Yuan, Z. Qiu, C. Wang, X. Zhang, Y. Ke, Y. Tang, Silicon-nanoparticle-based composites for advanced lithium-ion battery anodes, Nanoscale 12 (2020) 7461–7484, https://doi.org/10.1039/C9NR10652A.
[17] A. Fereydooni, C. Yue, Y. Chao, A brief overview of silicon nanoparticles as anode material: a transition from lithium-ion to sodium-ion batteries, Small 20 (2024) 2307275, https://doi.org/10.1002/smll.202307275.
[18] Z. Cheng, H. Jiang, X. Zhang, F. Cheng, M. Wu, H. Zhang, Fundamental understanding and facing challenges in structural design of porous Si-based anodes for lithium-ion batteries, Adv. Funct. Mater. 33 (2023) 2301109, https://doi.org/10.1002/adfm.202301109.
[19] Z.P. Guo, D.Z. Jia, L. Yuan, H.K. Liu, Optimizing synthesis of silicon/disordered carbon composites for use as anode materials in lithium-ion batteries, J. Power Sources 159 (2006) 332–335, https://doi.org/10.1016/j.jpowsour.2006.04.043.
[20] H. Wu, G. Zheng, N. Liu, T.J. Carney, Y. Yang, Y. Cui, Engineering empty space between Si nanoparticles for lithium-ion battery anodes, Nano Lett. 12 (2012) 904–909, https://doi.org/10.1021/nl203967r.
[21] D. Shao, D. Tang, J. Yang, Y. Li, L. Zhang, Nano-structured composite of Si/(S-doped-carbon nanowire network) as anode material for lithium-ion batteries, J. Power Sources 297 (2015) 344–350, https://doi.org/10.1016/j.jpowsour.2015.08.037.
[22] D. Wang, C. Zhou, B. Cao, Y. Xu, D. Zhang, A. Li, J. Zhou, Z. Ma, X. Chen, H. Song, One-step synthesis of spherical Si/C composites with onion-like buffer structure as high-performance anodes for lithium-ion batteries, Energy Storage Mater. 24 (2020) 312–318, https://doi.org/10.1016/j.ensm.2019.07.045.
[23] L. Cao, T. Huang, M. Cui, J. Xu, R. Xiao, Facile and efficient fabrication of branched Si@C anode with superior electrochemical performance in LIBs, Small 17 (2021) 2005997, https://doi.org/10.1002/smll.202005997.
[24] X. Meng, Z. Chen, J. Li, K.L. Harrison, W. Lu, X. Sun, Editorial for focus on nanophase materials for next-generation lithium-ion batteries and beyond, Nanotechnology 33 (2022) 410201, https://doi.org/10.1088/1361-6528/ac35d2.
[25] E.M. Lotfabad, P. Kalisvaart, K. Cui, A. Kohandehghan, M. Kupsta, B. Olsen, D. Mitlin, ALD TiO_2 coated silicon nanowires for lithium ion battery anodes with enhanced cycling stability and coulombic efficiency, Phys. Chem. Chem. Phys. 15 (2013) 13646–13657, https://doi.org/10.1039/C3CP52485J.
[26] N. Li, Z. Yi, N. Lin, Y. Qian, An Al_2O_3 coating layer on mesoporous Si nanospheres for stable solid electrolyte interphase and high-rate capacity for lithium ion batteries, Nanoscale 11 (2019) 16781–16787, https://doi.org/10.1039/C9NR05264J.
[27] J. Y. Huang, Y. Wang, G. T. Fei, S. H. Xu, B. Wang, Z. Zeng, Dual-functional antireflection and down-shifting coating for Si solar cells, Colloids Surf. A: Physicochem. Eng. Asp. https://doi.org/10.1016/j.colsurfa.2022.129907.
[28] Y. Ding, Z.P. Cano, A. Yu, J. Lu, Z. Chen, Automotive Li-ion batteries: current status and future perspectives, Electrochem. Energy Rev. 2 (2019) 1–28, https://doi.org/10.1007/s41918-018-0022-z.
[29] Z. Li, S. Zhao, J. Wang, X. Xian, Multi-component layer–protected Si-based composites with improved electrochemical performances as anode for Li-ion batteries, Ionics 30 (2024) 1319–1327, https://doi.org/10.1007/s11581-024-05374-y.
[30] M. Khan, S. Yan, M. Ali, F. Mahmood, Y. Zheng, G. Li, J. Liu, X. Song, Y. Wang, Innovative solutions for high-performance silicon anodes in lithium-ion batteries: overcoming challenges and real-world applications, Nano-Micro Lett. 16 (2024) 179, https://doi.org/10.1007/s40820-024-01388-3.
[31] L. Sun, Y. Liu, R. Shao, J. Wu, R. Jiang, Z. Jin, Recent progress and future perspective on practical silicon anode-based lithium ion batteries, Energy Storage Mater. 46 (2022) 482–502, https://doi.org/10.1016/j.ensm.2022.01.042.
[32] K.V. Baryshnikova, M.I. Petrov, V.E. Babicheva, P.A. Belov, Plasmonic and silicon spherical nanoparticle antireflective coatings, Sci. Rep. 6 (2016) 22136, https://doi.org/10.1038/srep22136.
[33] J. Li, J.-Y. Yang, J.-T. Wang, S.-G. Lu, A scalable synthesis of silicon nanoparticles as high-performance anode material for lithium-ion batteries, Rare Met. 38 (2019) 199–205, https://doi.org/10.1007/s12598-017-0936-3.
[34] D. Chen, W. Liao, Y. Yang, J. Zhao, Polyvinyl alcohol gelation: a structural locking-up agent and carbon source for Si/CNT/C composites as high energy lithium ion battery anode, J. Power Sources 315 (2016) 236–241, https://doi.org/10.1016/j.jpowsour.2016.03.051.
[35] S. Dhar, T. Dash, B.B. Palei, T.K. Rout, S.K. Biswal, A. Mitra, A.K. Sahu, S.K. Biswal, Silicon-graphene composite synthesis: microstructural, spectroscopic and electrical conductivity characterizations, Mater. Today: Proc. 33 (2020) 5136–5142, https://doi.org/10.1016/j.matpr.2020.02.858.
[36] A.S. Rajan, S. Sampath, A.K. Shukla, An in situ carbon-grafted alkaline iron electrode for iron-based accumulators, Energy Environ. Sci. 7 (2014) 1110–1116, https://doi.org/10.1039/C3EE42783H.
[37] J. Lilloja, M. Mooste, E. Kibena-Põldsepp, A. Sarapuu, B. Zulevi, A. Kikas, H.-M. Piirsoo, A. Tamm, V. Kisand, S. Holdcroft, A. Serov, K. Tammeveski, Mesoporous iron-nitrogen co-doped carbon material as cathode catalyst for the anion exchange membrane fuel cell, J. Power Sources Adv 8 (2021) 100052, https://doi.org/10.1016/j.powera.2021.100052.
[38] J. Luo, P. Xiao, Y. Li, J. Xiong, P. Zhou, L. Pang, X. Xie, Y. Li, Modified preparation of Si@C@TiO_2 porous microspheres as anodes for high-performance lithium-ion batteries, Dalton Trans. 52 (2023) 2463–2471, https://doi.org/10.1039/D2DT03775K.
[39] Y. Fu, Q. Yang, Three dimensional network Si–C composite coating constructed by porous skeletons as an integrated anode for lithium-ion batteries, J. Mater. Sci. 29 (2018) 15042–15051, https://doi.org/10.1007/s10854-018-9643-6.
[40] M. Phadatare, R. Patill, N. Blomquist, S. Forsberg, J. Örtegren, M. Hummelgård, J. Meshram, G. Hernández, D. Brandell, K. Leifer, S.K.M. Sathyanath, H. Olin, Silicon-nanographite aerogel-based anodes for high performance lithium ion batteries, Sci. Rep. 9 (2019) 1–9, https://doi.org/10.1038/s41598-019-51087-y.
[41] L. Shen, C. Xu, J. Gao, J. Tao, Q. Zhang, Y. Chen, Y. Lin, Z. Huang, J. Li, Scalable synthesized high-performance TiO_2-Si-C hybrid anode for lithium batteries, J. Energy Chem. 77 (2023) 348–358, https://doi.org/10.1016/j.jechem.2022.10.044.
[42] J. Li, Y. Huang, W. Huang, J. Tao, F. Lv, R. Ye, Y. Lin, Y.y. Li, Z. Huang, J. Lu, Simple designed micro–nano Si–graphite hybrids for lithium storage, Small 17 (2021) 2006373, https://doi.org/10.1002/smll.202006373.
[43] J. Wu, Y. Cao, H. Zhao, J. Mao, Z. Guo, The critical role of carbon in marrying silicon and graphite anodes for high-energy lithium-ion batteries, Carbon Energy 1 (2019) 57–76, https://doi.org/10.1002/cey2.2.
[44] J. Sung, N. Kim, J. Ma, J.H. Lee, S.H. Joo, T. Lee, S. Chae, M. Yoon, Y. Lee, J. Hwang, S.K. Kwak, J. Cho, Subnano-sized silicon anode via crystal growth inhibition mechanism and its application in a prototype battery pack, Nat. Energy 6 (2021) 1164–1175, https://doi.org/10.1038/s41560-021-00945-z.
[45] J.-B. Fang, Y.-Q. Cao, S.-Z. Chang, F.-R. Teng, D. Wu, A.-D. Li, Dual-design of nanoporous to compact interface via atomic/molecular layer deposition enabling a long-life silicon anode, Adv. Funct. Mater. 32 (2022) 2109682–2109693, https://doi.org/10.1002/adfm.202109682.
[46] Z. Xiao, C. Yu, X. Lin, X. Chen, C. Zhang, H. Jiang, R. Zhang, F. Wei, TiO_2 as a multifunction coating layer to enhance the electrochemical performance of SiO_x@TiO_2@C composite as anode material, Nano Energy 77 (2020) 105082, https://doi.org/10.1016/j.nanoen.2020.105082.
[47] N. Kirkaldy, M.A. Samieian, G.J. Offer, M. Marinescu, Y. Patel, Lithium-ion battery degradation: measuring rapid loss of active silicon in silicon–graphite composite electrodes, ACS Appl. Energy Mater. 5 (2022) 13367–13376, https://doi.org/10.1021/acsaem.2c02047.
[48] G.G. Eshetu, T. Diemant, S. Grugeon, R.J. Behm, S. Laruelle, M. Armand, S. Passerini, In-depth interfacial chemistry and reactivity focused investigation of lithium–imide- and lithium–imidazole-based electrolytes, ACS Appl. Mater. Interfaces 8 (2016) 16087–16100, https://doi.org/10.1021/acsami.6b04406.
[49] L. Gehrlein, C. Leibing, K. Pfeifer, F. Jeschull, A. Balducci, J. Maibach, Glyoxylic acetals as electrolytes for Si/Graphite anodes in lithium-ion batteries, Electrochim. Acta 424 (2022) 140642, https://doi.org/10.1016/j.electacta.2022.140642.
[50] X. Zhou, P. Li, Z. Tang, J. Liu, S. Zhang, Y. Zhou, X. Tian, FEC additive for improved SEI film and electrochemical performance of the lithium primary battery, Energies 14 (2021) 7467, https://doi.org/10.3390/en14227467.
[51] C.C. Nguyen, T. Yoon, D.M. Seo, P. Guduru, B.L. Lucht, Systematic investigation of binders for silicon anodes: interactions of binder with silicon particles and electrolytes and effects of binders on solid electrolyte interphase formation, ACS Appl. Mater. Interfaces 8 (2016) 12211–12220, https://doi.org/10.1021/acsami.6b03357.
[52] J. Chen, X. Fan, Q. Li, H. Yang, M.R. Khoshi, Y. Xu, S. Hwang, L. Chen, X. Ji, C. Yang, H. He, C. Wang, E. Garfunkel, D. Su, O. Borodin, C. Wang, Electrolyte design for LiF-rich solid–electrolyte interfaces to enable high-performance microsized alloy anodes for batteries, Nat. Energy 5 (2020) 386–397, https://doi.org/10.1038/s41560-020-0601-1.
[53] Y.C.G. Kwan, G.M. Ng, C.H.A. Huan, Identification of functional groups and determination of carboxyl formation temperature in graphene oxide using the XPS O 1s spectrum, Thin Solid Films 590 (2015) 40–48, https://doi.org/10.1016/j.tsf.2015.07.051.
[54] L. Madec, R. Petibon, J. Xia, J.P. Sun, I.G. Hill, J.R. Dahn, Understanding the role of prop-1-ene-1,3-sultone and vinylene carbonate in $LiNi_{1/3}Mn_{1/3}Co_{1/3}O_2$/graphite

pouch cells: electrochemical, GC-MS and XPS analysis, J. Electrochem. Soc. 162 (2015) A2635, https://doi.org/10.1149/2.0741512jes.
[55] Y. Bourlier, M. Bouttemy, O. Patard, P. Gamarra, S. Piotrowicz, J. Vigneron, R. Aubry, S. Delage, A. Etcheberry, Investigation of InAlN layers surface reactivity after thermal annealings: a complete XPS study for hemt, ECS J. Solid State Sci. Technol. 7 (2018) P329, https://doi.org/10.1149/2.0181806jss.
[56] H. Zhao, J. Li, Q. Zhao, X. Huang, S. Jia, J. Ma, Y. Ren, Si-based anodes: advances and challenges in Li-ion batteries for enhanced stability, Electrochem. Energy Rev. 7 (2024) 11, https://doi.org/10.1007/s41918-024-00214-z.